

Cross-shore stratified tidal flow seaward of a mega-nourishment

Meirelles, Saulo; Henriquez, Martijn; Reniers, Ad; Luijendijk, Arjen P.; Pietrzak, Julie; Horner-Devine, Alexander R.; Souza, Alejandro J.; Stive, Marcel J.F.

DOI

[10.1016/j.ecss.2017.10.013](https://doi.org/10.1016/j.ecss.2017.10.013)

Publication date

2018

Document Version

Accepted author manuscript

Published in

Estuarine, Coastal and Shelf Science

Citation (APA)

Meirelles, S., Henriquez, M., Reniers, A., Luijendijk, A. P., Pietrzak, J., Horner-Devine, A. R., Souza, A. J., & Stive, M. J. F. (2018). Cross-shore stratified tidal flow seaward of a mega-nourishment. *Estuarine, Coastal and Shelf Science*, 200, 59-70. <https://doi.org/10.1016/j.ecss.2017.10.013>

Important note

To cite this publication, please use the final published version (if applicable).
Please check the document version above.

Copyright

Other than for strictly personal use, it is not permitted to download, forward or distribute the text or part of it, without the consent of the author(s) and/or copyright holder(s), unless the work is under an open content license such as Creative Commons.

Takedown policy

Please contact us and provide details if you believe this document breaches copyrights.
We will remove access to the work immediately and investigate your claim.

Cross-shore stratified tidal flow seaward of a mega-nourishment

Saulo Meirelles^a, Martijn Henriquez^a, Ad Reniers^a, Arjen P. Luijendijk^{a,b},
Julie Pietrzak^a, Alexander R. Horner-Devine^c, Alejandro J. Souza^d, Marcel
J. F. Stive^a

^a*Department of Hydraulic Engineering, Delft University of Technology, Delft, the
Netherlands.*

^b*Deltares, Delft, the Netherlands.*

^c*Department of Civil and Environmental Engineering, University of Washington Seattle,
USA.*

^d*National Oceanography Center, Liverpool, the United Kingdom.*

Abstract

The Sand Engine is a 21.5 million m^3 experimental mega-nourishment project that was built in 2011 along the Dutch coast. This intervention created a discontinuity in the previous straight sandy coastline, altering the local hydrodynamics in a region that is influenced by the buoyant plume generated by the Rhine River. This work investigates the response of the cross-shore stratified tidal flow to the coastal protrusion created by the Sand Engine emplacement by using a 13 hour velocity and density survey. Observations document the development of strong baroclinic-induced cross-shore exchange currents dictated by the intrusion of the river plume fronts as well as the classic tidal straining which are found to extend further into the nearshore (from 12 to 6 m depth), otherwise believed to be a mixed zone. Estimates of the

*Saulo Meirelles

Email address: s.meirellesnunesdarocho@tudelft.nl (Saulo Meirelles)

centrifugal acceleration directly after construction of the Sand Engine showed that the curvature effects were approximately 2 times stronger, suggesting that the Sand Engine might have played a role in controlling the cross-shore exchange currents during the first three years after the completion of the nourishment. Presently, the curvature effects are minute.

Keywords: Baroclinic forcing, Centrifugal acceleration, Sand Engine, Cross-shore exchange currents

1. Introduction

In 2011, a localized mega-nourishment was implemented on the South-Holland coast, the Netherlands. This unique type of coastal protection, referred to as the Sand Engine or *Zandmotor* (in Dutch), was built in the shape of a hooked peninsula of $21.5 Mm^3$ of sand with initial dimensions of $2.4 \times 1 km$ in the along- and cross-shore directions respectively (Stive et al., 2013) (Figure 1). The Sand Engine is intended to naturally nourish the 17 km-long adjacent coast over a 20-year period, providing an environmental and economic solution to systematic coastal erosion. Despite being a soft-engineering intervention, the Sand Engine created a sharp discontinuity in the previously nearly alongshore uniform coast, which altered the typical hydrodynamic regimes (Huisman et al., 2016; Radermacher et al., 2016).

This artificial peninsula that characterizes the Sand Engine is expected to promote curvature-induced flow similar to that reported in the literature on river bend currents (e.g., Bathurst et al., 1977; Odgaard, 1986), flow around headlands (e.g., Gerret & Loucks, 1976; Geyer, 1993) and circulation in curved estuaries (e.g., Chant & Wilson, 1997; Lacy & Monismith, 2001).

Huisman et al. (2016) and Radermacher et al. (2016) have found that the alongshore barotropic tidal flow is substantially impacted by the Sand Engine as a result of flow contraction around the tip of the Sand Engine and flow separation at its flanks, however no information on the cross-shore (baroclinic) flow is provided. Because the barotropic alongshore (streamwise) current is deflected towards the outer bend, an imbalance between the depth-varying centrifugal acceleration and the cross-shore (cross-stream) pressure gradient is created, resulting in the development of cross-shore exchange currents (also referred as lateral, secondary or transverse flow). The cross-shore exchange currents are seaward-directed near the surface (towards the outer bend) and landward-directed near the bottom (Drinker, 1961). Such a pattern plays a role in the sediment transport, for example in rivers and estuaries where lateral sediment trapping has been observed due to curvature effects in combination with density gradients and Coriolis forcing (Geyer et al., 1998; Huijts et al., 2006; Fugate et al., 2007). Therefore, a clearer understanding of the role of curvature-induced cross-shore flow off the Sand Engine is important so as to evaluate if there is any feedback between the curvature of the shoreline perturbation and the evolution of the coastal profile.

Hydrodynamics along the South Holland coast are strongly influenced by the Rhine River ROFI (Region of fresh water Influence), which is generated by the discharge from the Rhine River through the Rotterdam waterways. Previous studies have described a pronounced baroclinic cross-shore circulation along the Dutch coast, in regions where the water column is stratified (Van der Giessen et al., 1990; Visser et al., 1994; De Boer et al., 2009). The cross-shore baroclinic pressure gradient is the main driver of the cross-shore

exchange currents controlling the orientation of the cross-shore circulation which switches every low water (LW) and high water (HW), owing to the effects of the cross-shore tidal straining (Souza & James, 1996). Tidal straining is a mechanism that results from the interaction of the vertical tidal shear and the horizontal density gradient, being responsible for inducing the semidiurnal switching of stratification (Simpson et al., 1993, 2005). As a result of straining, the Rhine ROFI is advected shoreward from HW to LW, whereas it is advected seaward from LW to HW (De Boer et al., 2008). The current structure and dynamics of river plumes has been studied extensively by Horner-Devine et al. (2015), however little attention has been paid to the modification of plume dynamics by coastline protrusions or the influence of the curvature-induced dynamics described above.

In general, the interaction between centrifugal acceleration and baroclinic pressure gradient may enhance or suppress the development of the cross-shore exchange currents. For example, the observations of Chant & Wilson (1997) near a headland in the Rudson River estuary revealed that the cross-shore density gradients weakened the centrifugally-induced flow resulting in an increase of the Ekman spin-down time of the tidally-generated eddies further downstream. Becherer et al. (2015) found, in the German Wadden Sea, that this interaction enhances the cross-shore exchange currents during flood and suppresses it during ebb. In the Marsdiep tidal inlet, the Netherlands, Buijsman & Ridderinkhof (2008) observed that the cross-shore exchange currents are mostly controlled by the centrifugal acceleration during flood and baroclinic forcing during ebb. In the Rhine ROFI system, under hypothetical conditions, the interplay between classic tidal straining and the centrifugal

acceleration seaward of the tip of the Sand Engine should enhance the cross-shore exchange currents from LW to HW and diminish it from HW to LW
70 as schematized in Figure 2. The verification of this hypothesis is discussed further in this work.

While there is established knowledge on cross-shore exchange currents, it is still uncertain how they occur around protruding beach nourishments. The Sand Engine, due to its unprecedented dimensions, provides a unique opportunity to gain insight on how cross-shore exchange currents interact with this
75 type of coastal intervention which have an erodible character. Furthermore, knowledge about the hydrodynamics is indispensable for understanding the evolution and role of the Sand Engine in nourishing the coast.

This paper investigates the cross-shore exchange currents around the Sand
80 Engine in the light of the major mechanisms responsible for controlling the cross-shore current structures. The main research question is: what is the response of the cross-shore stratified tidal flow to the perturbation created by the Sand Engine? Therefore, the interplay between baroclinic forcing and centrifugal acceleration on the development of cross-shore exchange currents
85 is examined. The objective is addressed through field measurements detailing the structure of the velocity and density fields immediately offshore of the Sand Engine.

2. Study area

The Sand Engine, built in 2011 with initial volume of $21.5Mm^3$ of sand,
90 is located along a sandy $17km$ stretch of the Dutch coast that is otherwise relatively straight (Figure 1). This domain has its southern limit bounded

by the Rotterdam waterways where the Rhine River discharges an average of $2200\text{ m}^3\text{ s}^{-1}$ of fresh water into the North Sea. The northern boundary is marked by the jetties of Scheveningen harbor.

95 The Sand Engine, which originally extended 1 km into the North Sea, has evolved dramatically since it was built. Within the first 2.5 years, the mega-nourishment redistributed 2.5 Mm^3 of sand (De Zandmotor, 2014) so that its morphology has consequently been changed from a hook shape into a Gaussian shape (de Schipper et al., 2016) (Figure 1a and c). Currently,
100 the Sand Engine extends 0.3 km perpendicular to the original coastline and 5 km in the alongshore. Evidently, the impact on the local hydrodynamics has reduced through this evolution and hence the curvature effects have also diminished. Below we describe the hydrodynamics in this region in the absence of the bathymetric perturbation associated with the Sand Engine.

105 The tide behaves as a Kelvin wave propagating from South to North along the Dutch coast so that the peak of flood currents coincides with HW so does the peak of ebb currents with LW. The orientation of tidal ellipses generally follows the isobaths (Van der Giessen et al., 1990). The semi-diurnal band, which is dominated by the M_2 constituent, holds about 90%
110 of the variance of the tidal signal. The near surface M_2 amplitude ($\approx 4\text{ m}$ below the surface) increases seaward over a cross-shore distance of about 10 km (from ≈ 55 to $\approx 60\text{ cms}^{-1}$), while the near bottom amplitudes ($\approx 4\text{ m}$ above the bottom) decreases (from ≈ 43 to $\approx 32\text{ cms}^{-1}$) (Visser et al., 1994). The peak of flood and ebb currents fluctuates typically 30% over an entire
115 spring-neap cycle (Visser et al., 1994). The largest shallow-water constituent in the northeast European shelf is the M_4 with average amplitudes higher

than 8 *cm* (Andersen, 1999).

In the North Sea, the vertical structure of the tidal current is affected by differences in eddy viscosity over depth owing to stratification (Maas & Van Haren, 1987). Visser et al. (1994) demonstrated how the suppression of turbulence at the pycnocline leads to a significant increase of the cross-shore tidal current that can reach 35 cm s^{-1} in the Rhine River ROFI. The later investigation from Souza & Simpson (1996) confirmed the enhancement of the cross-shore amplitudes by showing that the tidal current ellipses develop a more circular pattern with the onset of stratification.

Van der Giessen et al. (1990) observed a large variability of residual currents along the Dutch coast which closely correlates with fluctuations of the wind field on time scales of days to weeks. If persistent, northeasterly winds can enhance stratification, while southwesterly winds favor mixing (Souza & James, 1996). The results presented by Souza & Simpson (1996) showed that winds are the main agent in controlling stratification in the Rhine region of influence. The stability of the vertical density structure is also dictated by tidal and wave stirring (Souza & Simpson, 1997).

The wave climate along the Dutch coast is dominated by wind-sea waves. Under typical conditions, they approach the coast from the western quadrant and swell is primarily from northwesterly direction due to the geometry of the North Sea (Wijnberg, 2002). The nearshore wave climate varies considerably and is characterized by waves of moderate height and short period (Van Rijn, 1997). The wave action on the South-Holland coast is the main driver of the Sand Engine evolution followed by the tidal flow (Luijendijk et al., 2017).

3. Methods

A 13-hour field campaign was conducted to map the cross-shore current structures and the density field in order to investigate how the baroclinic forcing and centrifugal acceleration control the cross-shore exchange currents
145 in the study area.

3.1. Field campaign

The measurement of current velocities was conducted on October 17, 2014 over two transects perpendicular to the original (unnourished) coastline (Figure 1). Transect 1 (T1) was aligned with the tip of the Sand Engine and
150 transect 2 (T2) was located at its northern flank. Concurrently, the density structure of the water column was measured at the beginning and the end of every transect. The sampling strategy envisioned to capture the mechanisms that generates cross-shore exchange currents on the time-scale of the semi-diurnal tide ($\approx 12.5 h$). The analysis of the balance between centrifugal
155 acceleration and baroclinic forcing focuses on the T1 transect because it is radial to the Sand Engine curvature.

An ADCP Workhorse 600 KHz , looking downward, with sampling frequency of $0.6 Hz$, was mounted on a boat and integrated into a DGPS system able to correct accurately for the pitch, roll and heading. The ADCP's main
160 axis pointed 45° to the boat's bow allowing all beams to detect a similar magnitude of Doppler shift with the aim of increasing accuracy (Raye & Driscoll, 2002). The ADCP was positioned $1 m$ below the waterline.

During a semi-diurnal tidal cycle, the boat navigated over the transects in a clockwise direction at a speed of about $2 m s^{-1}$. The transects were

165 640 m apart from each other so that the surveying time of two consecutive
transects was short enough that the statistical distribution of the tidal flow
did not significantly change within this interval. Both transects had their
offshore and onshore limits roughly between the isobaths of -12 and -5 m ,
respectively. The ADCP was set to measure over 20 m depth with a vertical
170 resolution of 0.5 m comprising 40 measurement cells.

The density profiles were obtained with a Castaway-CTD. This instru-
ment features built-in GPS that gives the geographic position. The CTD
sampled at 5 Hz which provided enough vertical resolution to capture verti-
cal density stratification associated with the Rhine River plume at the site.
175 From 1100H to 1500H, additional CTD casts were carried out from a jet-ski
to increase the cross-shore resolution at T1.

3.2. ADCP data processing

The ADCP dataset consists of 56 transect repetitions and the average
time between each repetition was 24 minutes. The velocities measured at
180 T1 and T2 were rotated to a coordinate system aligned with the main coast-
line orientation of 42° . Thus the cross- (u) and alongshore (v) components
of the velocities could be resolved. Subsequently, a moving average with a
window of 3 profiles was applied to reduce noise. The navigated transects
were projected onto reference transects T1 and T2 through the inverse dis-
185 tance weighting method that spanned over the two closest neighbors. This
procedure was repeated for each depth creating a 2D grid with horizontal
and vertical resolution of $\Delta x = 0.7$ m and $\Delta z = 0.5$ m , respectively.

Following the analysis of Valle-Levinson et al. (2015), the M_2 tidal con-
stituent was extracted from the series of horizontal velocities by using least-

190 squares-based harmonic analysis (Codiga, D. L., 2011) in which the velocities were represented as complex numbers ($u + iv$). Later the data was smoothed by applying a moving average with 90 m window along the transects. In addition, the remaining spurious values, i.e spikes, were manually removed from the series.

195 3.3. Tidal current ellipses

Because the properties of the vertical structure of the M_2 tidal current ellipses are modified by stratification (e.g., Souza & Simpson, 1996; van Haren, 2000), the ellipse parameters were calculated. These were derived from the complex velocities which were decomposed, for a specified frequency, into cy-
 200 clonic and anti-cyclonic circular components with amplitudes W_{\pm} and phases θ_{\pm} (Thomson & Emery, 2014). The semi-major axis (U), phase angle (ϕ) and the ellipticity (also referred to as eccentricity) (ε) of the ellipses are expressed, respectively, by:

$$U = W_+ + W_-, \quad (1)$$

$$\phi = (\theta_- - \theta_+)/2, \quad (2)$$

$$\varepsilon = (W_+ - W_-)/(W_+ + W_-). \quad (3)$$

The semi-major axis indicates the maximum current velocity, the phase
 205 defines the time taken to reach the maximum current, the ellipticity determines if the tidal motion is rectilinear ($\varepsilon = 0$; i.e the semi-minor axis of the tidal ellipses have a negligible amplitude) or circular ($\varepsilon = 1$) and the sign

of the ellipticity provides the sense of rotation (negative is anti-cyclonic and positive is cyclonic).

210 *3.4. Cross-shore exchange currents*

In order to evaluate the impact of the Sand Engine’s curvature on the hydrodynamics, it is necessary to compare the cross-shore exchange currents generated by centrifugal acceleration with those induced by baroclinic forcing. We will make this comparison based on the two-layer momentum balance
215 described below.

The dynamics of the cross-shore exchange currents associated with curvature are commonly analyzed through the approach by Kalkwijk & Booij (1986) who presented an analytic solution for the momentum balance equation for curved flows. This method determines the generation of secondary
220 flow that is forced by curvature as well as Coriolis acceleration. The reduction of the eddy viscosity, A , by stratification is not accounted for, which may modify the strength of the cross-shore exchange currents as reported by Geyer (1993).

To examine the role of stratification on the cross-shore exchange currents, Seim & Gregg (1997) included the baroclinic pressure term in the secondary flow governing equation of Kalkwijk & Booij (1986):

$$\frac{\partial u}{\partial t} + v \frac{\partial u}{\partial y} + \frac{v^2 - \langle v^2 \rangle_z}{R} = -\frac{g}{\rho_0} \int_z^0 \frac{\partial \rho}{\partial x} dz + \frac{g}{\rho_0} \frac{\partial \langle \rho \rangle_z}{\partial x} h + \frac{\partial}{\partial z} \left(A \frac{\partial u}{\partial z} \right) + \frac{\tau_b}{\rho h}, \quad (4)$$

where x , y and z denote the cross-shore, alongshore and vertical coordinates, respectively. R is the local radius of curvature and h is the water depth.
225 Depth-averaged quantities are denoted by $\langle \rangle_z$. The acceleration due to

gravity is represented by g , ρ_0 is a constant reference water density, ρ is the seawater density and τ_b is the cross-shore bottom stress.

Seim & Gregg (1997) scaled Equation 4 by assuming a steady balance between centrifugal acceleration and the cross-shore (or cross-channel) baroclinic pressure gradient, simplifying it to:

$$\frac{v^2 - \langle v^2 \rangle_z}{R} = -\frac{g}{\rho_0} \int_z^0 \frac{\partial \rho}{\partial x} dz + \frac{g}{\rho_0} \frac{\partial \langle \rho \rangle_z}{\partial x} h. \quad (5)$$

The omission of frictional forces in Equation 5 was justified by considering
 230 the relative importance of advection to friction. The ratio of these terms is defined as $R_{ef} = h/LC_D \sim v \frac{\partial u}{\partial y} / \frac{\tau_b}{\rho h}$, where R_{ef} is the equivalent Reynolds number, L is the alongshore (streamwise) length scale and C_D is the bottom drag coefficient Alaei et al. (2004), and values of $R_{ef} > 1$ indicates that friction is of secondary importance. The values of R_{ef} were 1.68 ± 0.35 during
 235 our measurement period (not shown), confirming that advective processes prevailed over bottom friction and we have thus left out the frictional terms. Given the dimensions of the Sand Engine, Coriolis acceleration is assumed to be irrelevant as the Rossby number, $2v/fR$, is greater than unity (≈ 3), i.e, curvature effects dominate over Coriolis.

240 To calculate the centrifugal acceleration (LHS of Equation 5), the ADCP velocities were first divided in two layers of equal height following the bathymetry of the cross-shore profile, then the centrifugal acceleration was computed and averaged over each layer separately. The values of the bottom layer were then subtracted from those of the top layer following the approach by Buijsman &
 245 Ridderinkhof (2008), eliminating the barotropic pressure gradient from the balance. Using this same two-layer approach, the baroclinic forcing (RHS of Equation 5) was calculated with the CTD data and compared with the

centrifugal acceleration (LHS of Equation 5).

4. Observations

250 The measurements took place during neap tide which is the part of the
spring-neap cycle typically characterized by strong stratification. This strong
stratification results from the reduced vertical mixing due to tidal stirring
that is generated by the weaker neap currents. The river discharge was
about $1651\text{ m}^3\text{ s}^{-1}$ which is below the annual mean that is between 2000 and
255 $2500\text{ m}^3\text{ s}^{-1}$. Winds and waves were approximately orthogonal to each other
and developed a choppy sea state during the survey. Waves were measured
by a wave buoy deployed at the site. The root-mean-squared wave height,
 H_{rms} , was slightly higher than 0.4 m throughout the survey and the wave di-
rection was nearly perpendicular to the shore. The mean Stokes drift was of
260 0.012 m s^{-1} near the surface and negligible near the bottom. The meteorolog-
ical station in Rotterdam registered persistent SW winds fluctuating from 5
to 8 m s^{-1} . The depth-averaged wind-generated current, based on the Ekman
motion, was shore-directed with average speed of 0.044 m s^{-1} . We anticipate
that the Stokes drift and wind-driven current were neglected in the analysis of
265 the cross-shore exchange currents. The Stokes drift presented very small val-
ues and it did not contribute to the development of the cross-shore exchange
currents. Regarding the role of the winds, they can significantly modify the
flow and dynamics of the Rhine ROFI, however their directly influence on
the development of the cross-shore exchange currents in the shallow regions
270 of the inner shelf and nearshore considered in this paper are not well studied.
Our calculations for the study period show that the cross-shore exchange is

strongly dominated by the density gradient. While wind-generated currents are likely to be dominant during high wind events, we anticipate that the cross-shore exchange currents are not forced by the wind-generated currents and therefore the winds do not control the cross-shore exchange currents.

The presence of cross-shore exchange currents is apparent from the vertical decoupling of the cross-shore component of the tidal currents (Figures 3e and f) marked by a 180° phase shift from top to bottom. The maximum cross-shore currents occurred during the period of strong stratification reaching offshore and onshore velocities of -24 and 20 cm s^{-1} , respectively. The observed cross-shore exchange currents extended to the shallower part of T1 (Figure 3g), although the cross-shore velocities were significantly smaller (-8 and 11 cm s^{-1}). The vertical density structure and the velocities at T2 is also presented in Figure 3 for comparison purposes.

The alongshore component behaved as expected (i.e, with the characteristics of a progressive Kelvin wave) and therefore the alongshore tidal currents were approximately in phase with the water elevation (Figures 3a, b, c and d). The alongshore currents reached 66 cm s^{-1} and -55 cm s^{-1} during flood and ebb, respectively. The velocities observed at the shoreward limit of T1 were higher than those of T2, indicating that the contraction of the tidal current as it flows around the tip of the Sand Engine (Radermacher et al., 2016).

The observed density structures showed a clear variability of strong vertical stratification from LW to HW (Figures 3i and k). After HW, the stratification started to weaken substantially, but the water column was not fully mixed. The water density near the bottom varied from 1020.80

to 1022.75 kgm^{-3} and from 1020.39 to 1022.08 kgm^{-3} at the seaward and shoreward limits of T1, respectively. Near the surface those values varied from 1020.04 to 1021.33 kgm^{-3} and from 1020.06 to 1021.59 kgm^{-3} .

300 The variability of the cross-shore density field is illustrated in Figure 4 for two distinct periods. The first is just after HW when water column was de-stratifying and the cross-shore velocity profile exhibited relatively strong offshore-directed velocities in the lower layer of the water column and onshore-directed velocities in the upper layer (Figure 4a). The second is dur-
305 ing early ebb when the water column became slightly stratified again (Figure 4b) and the associated cross-shore velocity profile exhibited onshore-directed velocities in the lower layer of the water column and offshore-directed velocities in the upper layer. The variability of the density field is also captured by radar images that showed the recurrent presence of the plume front during
310 the measurements (Figures 4c to f) and therefore vertical stratification was observed much of the time (Figures 4g to j).

The Richardson number, Ri , defined as the ratio of the buoyancy frequency, $N^2 = (-g/\rho_0) \partial\rho/\partial z$ to the squared vertical shear, $S^2 = (\partial u/\partial z)^2 + (\partial v/\partial z)^2$ (i.e, $Ri = N^2/S^2$), provides information on the competition be-
315 tween shear-driven mixing and vertical density stratification. Figures 5c and f show time series of the transformed Richardson number ($\log(4Ri)$) calculated for the offshore and onshore limits of T1. The values of $\log(4Ri)$ were above the threshold for stability ($\log(4 \cdot 0.25) = 0$) most of the tidal cycle indicating a tendency for the development of stratification. Given this con-
320 dition, the turbulent mixing tends to be reduced or, as Geyer et al. (1998) pointed out, the shear may be enhanced by stratification. The results showed

moments of high vertical shear (Figures 5a and d) coinciding with the stratified period (Figures 5b and e) which may imply that shear is intensified by stratification, consistent with the model of Visser et al. (1994).

325 Figure 6 displays the vertical shear of the u component ($\partial u/\partial z$) computed with the M_2 tidal velocities averaged over 30 *min* bins. The vertical shear ranged from -0.24 to 0.16 s^{-1} in which negative and positive values indicate a tendency of counterclockwise (CC) and clockwise (CW) rotation in the vertical plane. From LW to HW, during the period of strong stratification, 330 the cross-shore circulation tended to rotate in the CC direction. After HW, when stratification started to break down, the vertical shear changed sign, meaning that the sense of rotation of the cross-shore circulation tended to be in the CW direction. At about 1400H, the circulation changed sign again so that it was predominately in the CC direction. This period coincides with 335 the approximation of the plume front as shown by the radar images in Figure 4c to f.

The amplitude, phase and ellipticity of the M_2 tidal constituent derived from the harmonic analysis are shown in Figure 7. In general, the observed amplitudes and phases of the M_2 constituent were uniform throughout T1. 340 The results for the ellipticity of the M_2 constituent showed an anti-cyclonic rotating ellipses near the surface and cyclonic rotating ellipses near the bottom all over the surveyed transect. These results agree with the findings of (Souza & Simpson, 1996) who reported changes of the tidal ellipse parameters over depth due to the influence of the Rhine ROFI. We additionally showed 345 that the modification of the tidal ellipses in the presence of stratification can extend further into the nearshore.

5. Discussion

The results from the observations presented in Section 4 identify the cross-shore current structures seaward of the Sand Engine along Transect T1. In this Section, the role of the density gradients and curvature in yielding cross-shore exchange currents is explored focusing on how the presence of the mega-nourishment results in changes of cross-shore circulation.

The strong vertical stratification captured in the measurements is part of the semi-diurnal switching of stratification that has been extensively investigated in the Rhine River ROFI (Visser et al., 1994; Simpson & Souza, 1995; Souza & Simpson, 1996, 1997; De Boer et al., 2006, 2008, 2009). The present work showed that this mechanism extends to the nearshore zone (up to ≈ 6 m depth) despite the perturbation of the tidal flow caused by the Sand Engine as well as the stirring by wind and waves, which are expected to maintain the nearshore zone permanently well-mixed as suggested by De Boer et al. (2009). The observations revealed a close association between stratification and the cross-shore flow (Figure 3). The semi-diurnal variability of the density field is attributed to classic cross-shore tidal straining due to the two-way interaction between horizontal density gradient and the counter-rotating tidal ellipses, resulting in the semidiurnal switching in stratification as described by (Simpson & Souza, 1995). The proximity of the measurement site to the Rhine outflow likely explains why stratification was observed in the nearshore, because the effects of tidal straining are enhanced due to the larger amount of fresh water that can be advected towards the coast (Simpson et al., 1993). Moreover, during periods when a larger amount of fresh water is advected to the coast, other baroclinic processes rather than tidal strain-

ing are responsible for generating additional vertical stratification (De Boer et al., 2008; Flores et al., 2017). Likewise, the observed stratification during ebb (about 1400H) cannot be explained by the semi-diurnal switching
375 of stratification (tidal straining) and thus other baroclinic processes might have taken place due to the presence of the Rhine ROFI at the site during the survey. (Figures 3 and 4). The frontal processes, that are inherent to the near-field of the river plume (De Boer et al., 2008), also controlled the cross-shore exchange currents. Under these conditions, the buoyancy input
380 may prevail over the stirring processes by wind and waves seaward of the Sand Engine during fair-weather conditions.

The results for the Richardson number (Figure 5) indicated that stratification had a dominant influence on the vertical structure of the flow measured at T1. Further evidence of this dominance is shown by the ellipticity of the
385 M_2 constituent (Figure 7e) which is strongly controlled by stratification as demonstrated by Souza & Simpson (1996). The ellipticity of the M_2 constituent clearly showed the decoupling of the water column in two layers, denoting the importance of stratification in yielding the observed cross-shore exchange currents which extended all over the surveyed transect. This con-
390 dition is believed to be representative of longer timescales as the average stratification (top-to-bottom salinity differences) from a six week mooring deployment during the same time period was $2.14 \pm 1.7 \text{ psu}$ (Flores et al., 2017) while the average stratification on October 17, 2014 was 2.29 psu .

To analyze the interplay between centrifugal acceleration and the baro-
395 clinic pressure gradient, Eq. 5 was scaled as in Seim & Gregg (1997) but using the two-layer approach so that the centrifugal term and the baroclinic

forcing became $\Delta(v^2/R)$ and $(m/B)(gh/\rho_0)\Delta\rho$, respectively, where B is the transect width and $\Delta\rho$ is the top-to-bottom density differences and m gives the sign of the baroclinic forcing based on the mean cross-shore slope of the isopycnals. These calculations showed that the buoyancy force was greater than the centrifugal acceleration during the 13-hours survey (Figure 8a). The strength of the vertical shear (Figure 6) appeared to be controlled by $(m/B)(gh/\rho_0)\Delta\rho$ (Figure 8) confirming the minute role of the curvature effects either in counteracting or enhancing the cross-shore exchange currents. After HW slack, weak vertical stratification was observed (Figure 3i) as the plume front approximated to the nearshore zone (Figure 4e) causing a switch of the cross-shore exchange currents at T1 but not at T2 (Figures 3e and f). At this tidal phase, the centrifugal acceleration was very small and thus it is plausible that the cross-shore baroclinic forcing was controlled by other baroclinic processes rather than classic tidal straining (i.e., semi-diurnal switching of stratification) so that the vertical shear tended to maintain a CC circulation at T1.

As the centrifugal acceleration is a function of the alongshore velocities and the radius of curvature, it should fluctuate not only over a spring-neap cycle but also, on a longer timescale, according to the pace that the Sand Engine flattens out. We consider here whether the centrifugal acceleration played a more significant dynamical role immediately after the Sand Engine was built when the curvature was greater. The centrifugal acceleration in prior conditions was estimated by using the radius of curvature of the Sand Engine estimated from bathymetric surveys in each year since 2011 and two weeks of simulated velocities off the tip of the Sand Engine (see Luijendijk

et al., 2015). In this estimate it was assumed that the flow contraction at the tip does not lead to any significant increase of the alongshore velocities at 12 *m* depth, resulting in a conservative estimate of the magnitude of the centrifugal term. In Figure 8i the centrifugal acceleration estimates are compared with the range of baroclinic forcing observed during our sampling period, noting that this corresponds to a neap period when the stratification is generally high. This exercise suggests that the curvature likely played a more important role in the first three years of the Sand Engine. At that time, the magnitudes of the centrifugal acceleration were comparable to the baroclinic forcing, although the mean baroclinic forcing was still higher than the mean centrifugal acceleration. Nonetheless, the cross-shore exchange currents might also have been controlled by curvature effects especially during spring tides, when stronger currents strengthen the centrifugal acceleration and tidal stirring reduces the baroclinic forcing.

Presently, the seaward deflection of the alongshore currents due to the curvature around the tip of the Sand Engine does not contribute significantly to the development of the observed cross-shore exchange currents. Given the observed dominance of the baroclinic forcing, the hypothetical interplay between centrifugal acceleration and baroclinic forcing seen in Figure 2 may be only valid in the far-field of the Rhine ROFI where the cross-shore baroclinic pressure gradient is expected to be controlled solely by the classic tidal straining and, obviously, where a curved seaward protrusion, such as the Sand Engine in its early stages, is present.

Therefore, as the cross-shore exchange currents did not appear to be effectively forced by centrifugal acceleration, we performed a scaling analysis

of the remaining terms of Equation 4 to determine whether they contribute to the cross-shore momentum balance. Apart from centrifugal acceleration and baroclinic forcing, we also included the advective acceleration, $\Delta(uv/L)$, Coriolis acceleration, $\Delta(fu)$, vertical dissipation, $\Delta(Au/h^2)$, and time variation, $\Delta u/\Delta t$. The results in Figure 8j clearly demonstrated how the cross-shore exchange currents were greatly governed by fluctuations of the baroclinic pressure gradient (black bars in Figure 8j), while the contribution of the other terms appeared to not significantly affect the behavior of the cross-shore exchange currents.

Nonetheless, the magnitude of the term $\Delta u/\Delta t$ (i.e., local time variation) revealed there is a tendency for the flow to accelerate (magenta bars in Figure 8j), implying the existence of a local imbalance between the driving forces. Thus, the time needed reach a steady state balance in Equation 5, as discussed by (Lacy & Monismith, 2001), could not be achieved most likely due to the short time that the tide takes to flow around the tip of the Sand Engine. Yet, it is not entirely clear whether other terms might have come to play with respect to the momentum balance. A speculative explanation is that the downwards transfer of momentum due to Reynolds stresses associated with the wave motion (i.e., $\overline{\rho\tilde{u}\tilde{w}} \neq 0$) (see Nielsen et al., 2011) might have contributed to the mixing term of the momentum balance as shore-perpendicular irregular waves were observed during the survey. However, with the available dataset, it was not possible to describe the term $\overline{\rho\tilde{u}\tilde{w}}$.

Moreover, the estimation of horizontal gradients over shallow and sloping bathymetries imposes a number of constraints ranging from numerical problems (e.g., Stelling & Van Kester, 1994) to observational limitations (e.g.,

Hopkins, 1996). Hence, the scaling used in the present study, in which the baroclinic forcing is calculated from density profiles of two stations of unequal depth, provides a first-order approximation of the baroclinic term in
475 Equation 5. Although the two-layers approach minimized some of those restrictions, it is likely that the assumption of mild cross-shore density gradients is violated when the plume front propagated through the surveyed transects around 1130H.

6. Conclusions

480 The observational results presented here provided information on the cross-shore current structures seaward of the Sand Engine, a localized mega-nourishment meant to naturally supply sand to the adjacent coast. Despite the large perturbation of the coastline, the current curvature of the Sand Engine does not present an appreciable contribution in controlling the cross-
485 shore exchange currents. However, the curvature of the Sand Engine was higher when it was first built. Estimates of the centrifugal acceleration with higher curvature conditions suggest that curvature played a more significant role in the local dynamics during the first three years after the Sand Engine was built, and likely contributed to cross-shore exchange currents. These
490 effects are further enhanced during spring tides.

The cross-shore exchange currents were found to be strongly driven by the cross-shore baroclinic pressure gradient in the study area. The observed centrifugal accelerations were not large enough to balance the cross-shore baroclinic pressure gradient, thus other accelerations, e.g., $\Delta u/\Delta t$, are re-
495 quired to produce a balance considering the local spatiotemporal scale. The

wave motion of the shoaling waves is believed to contribute to this balance, although it was not possible to quantify the competition between wave stirring and stratification in the nearshore.

Nonetheless, the occurrence of stratification in depths as shallow as 6 m associated with a relatively strong cross-shore shear, revealed that tidal straining and other baroclinic processes can occur in shallow waters even under the stirring effects of waves and wind. The proximity to the Rhine River mouth is a key condition that allows these baroclinic processes to take place in the nearshore.

Finally, the dataset used in this work, although limited, served to interpret the governing mechanisms of the cross-shore current structures in the vicinity of the Sand Engine. These findings strongly suggest that planning for future large nourishment projects such as the Sand Engine should consider the proximity of freshwater inflows to the nourishment site and account for the dynamics of the stratification-induced circulation in the nourishment design. This is an especially important consideration since good nourishment sites may often be proximate to large river inflows as engineered river mouths can often interrupt longshore sediment transport.

7. Acknowledgments

The authors would like to thank the EU Research Council for funding this research through the ERC-advanced grant 291206 Nearshore Monitoring and Modeling (NEMO) and the Netherlands Organisation for Scientific Research STW program Project 12682 Sustainable Engineering of Coastal Systems in Regions of Freshwater Influence. The authors are indebted to the

520 MegaPEX coordinators for providing all the necessary logistic for the field
work. Our gratitude to George Fotis for his valuable help in the field. We also
wish to thank Rijkswaterstaat, Cpt. Daan Wouwenaar and Ronald Brouwer.
Bas Hoonhout and Howard Southgate contributed with valuable comments
on the draft. The anonymous reviewers contributed enormously with their
525 comments. Bas Huisman is thanked for his help with the s-coordinates trans-
formation. Mini, Yang and Bel are heartfelt thanked for all unconditional
support to SM.

References

- Alaee, M. J., Ivey, G., & Pattiaratchi, C. (2004). Secondary circulation
530 induced by flow curvature and coriolis effects around headlands and islands.
Ocean Dynamics, *54*, 27–38.
- Andersen, O. B. (1999). Shallow water tides in the northwest european
shelf region from topex/poseidon altimetry. *Journal of Geophysical Re-
search: Oceans*, *104*, 7729–7741. URL: [http://dx.doi.org/10.1029/
535 1998JC900112](http://dx.doi.org/10.1029/1998JC900112). doi:10.1029/1998JC900112.
- Bathurst, J. C., Thorne, C. R., & Hey, R. D. (1977). Direct measurements
of secondary currents in river bends. *Nature*, *269*, 504–506. doi:<http://dx.doi.org/10.1038/269504a0>.
- Becherer, J., Stacey, M. T., Umlauf, L., & Burchard, H. (2015). Lateral
540 circulation generates flood tide stratification and estuarine exchange flow
in a curved tidal inlet. *Journal of Physical Oceanography*, *45*, 638–656.

- Buijsman, M., & Ridderinkhof, H. (2008). Variability of secondary currents in a weakly stratified tidal inlet with low curvature. *Continental Shelf Research*, 28, 1711 – 1723. URL: <http://www.sciencedirect.com/science/article/pii/S0278434308001520>.
545 doi:<http://dx.doi.org/10.1016/j.csr.2008.04.001>.
- Chant, R. J., & Wilson, R. E. (1997). Secondary circulation in a highly stratified estuary. *Journal of Geophysical Research: Oceans*, 102, 23207–23215. URL: <http://dx.doi.org/10.1029/97JC00685>. doi:10.
550 1029/97JC00685.
- Codiga, D. L. (2011). *Unified tidal analysis and prediction using the UTide Matlab functions (Python version)*. Technical Report 2011-01 University of Rhode Island Graduate School of Oceanography, University of Rhode Island, Narragansett, RI.
- 555 De Boer, G. J., Pietrzak, J. D., & Winterwerp, J. C. (2006). On the vertical structure of the Rhine region of freshwater influence. *Ocean dynamics*, 56, 198–216.
- De Boer, G. J., Pietrzak, J. D., & Winterwerp, J. C. (2008). Using the potential energy anomaly equation to investigate tidal straining and advection
560 of stratification in a region of freshwater influence. *Ocean Modelling*, 22, 1–11.
- De Boer, G. J., Pietrzak, J. D., & Winterwerp, J. C. (2009). SST observations of upwelling induced by tidal straining in the Rhine ROFI. *Continental Shelf Research*, 29, 263 – 277. URL: [25](http://</p></div><div data-bbox=)

- 565 www.sciencedirect.com/science/article/pii/S0278434307001847.
doi:<http://dx.doi.org/10.1016/j.csr.2007.06.011>. Physics of
Estuaries and Coastal Seas: Papers from the PECS 2006 Conference.
- De Zandmotor (2014). *The Sand Motor: looking back at 2.5 years of
building with nature*. Technical Report Rijkswaterstaat. URL: [http:
570 //www.dezandmotor.nl](http://www.dezandmotor.nl).
- Drinker, P. (1961). *Boundary shear stresses in curved trapezoidal channels*.
Ph.D. thesis Massachusetts Institute of Technology.
- Flores, R. P., Rijnsburger, S., Horner-Devine, A. R., Souza, A. J., & Pietrzak,
J. D. (2017). The impact of storms and stratification on sediment trans-
575 port in the rhine region of freshwater influence. *Journal of Geophysical
Research: Oceans*, . URL: <http://dx.doi.org/10.1002/2016JC012362>.
doi:10.1002/2016JC012362.
- Fugate, D. C., Friedrichs, C. T., & Sanford, L. P. (2007). Lateral dynamics
and associated transport of sediment in the upper reaches of a partially
580 mixed estuary, Chesapeake Bay, USA. *Continental Shelf Research*, 27, 679
– 698. doi:<http://dx.doi.org/10.1016/j.csr.2006.11.012>.
- Gerret, C. J. R., & Loucks, R. H. (1976). Upwelling along the Yarmouth
shore of Nova Scotia. *J. Fish. Res. Board of Can.*, 33, 116–117.
- Geyer, W. R. (1993). Three-dimensional tidal flow around headlands. *Journal
585 of Geophysical Research: Oceans (1978–2012)*, 98, 955–966.
- Geyer, W. R., Signell, R. P., & Kineke, G. C. (1998). Lateral trapping of
sediment in a partially mixed estuary. In J. Dronkers, & M. B. A. M.

- Scheffers (Eds.), *Physics of Estuaries and Coastal Seas* chapter 2. (pp. 115–124).
- 590 Van der Giessen, A., De Ruijter, W., & Borst, J. (1990). Three-dimensional current structure in the Dutch coastal zone. *Netherlands Journal of Sea Research*, *25*, 45–55.
- van Haren, H. (2000). Properties of vertical current shear across stratification in the North Sea. *Journal of Marine Research*, *58*, 465–491.
- 595 Hopkins, T. S. (1996). A note on the geostrophic velocity field referenced to a point. *Continental Shelf Research*, *16*, 1621 – 1630. URL: <http://www.sciencedirect.com/science/article/pii/0278434395000801>. doi:[http://dx.doi.org/10.1016/0278-4343\(95\)00080-1](http://dx.doi.org/10.1016/0278-4343(95)00080-1).
- Horner-Devine, A. R., Hetland, R. D., & MacDonald, D. G. (2015). Mixing and transport in coastal river plumes. *Annual Review of Fluid Mechanics*, 600 *47*, 569–594.
- Huijts, K. M. H., Schuttelaars, H. M., de Swart, H. E., & Valle-Levinson, A. (2006). Lateral entrainment of sediment in tidal estuaries: An idealized model study. *Journal of Geophysical Research: Oceans*, 605 *111*. URL: <http://dx.doi.org/10.1029/2006JC003615>. doi:10.1029/2006JC003615. C12016.
- Huisman, B., de Schipper, M., & Ruessink, B. (2016). Sediment sorting at the sand motor at storm and annual time scales. *Marine Geology*, (pp. –). URL: <http://www.sciencedirect.com/science/article/pii/>

610 S0025322716301918. doi:<http://dx.doi.org/10.1016/j.margeo.2016.09.005>.

Kalkwijk, J. P. T., & Booij, R. (1986). Adaptation of secondary flow in nearly-horizontal flow. *Journal of Hydraulic Research*, *24*, 19–37. doi:10.1080/00221688609499330.

615 Lacy, J. R., & Monismith, S. G. (2001). Secondary currents in a curved, stratified, estuarine channel. *Journal of Geophysical Research: Oceans*, *106*, 31283–31302.

Luijendijk, A. P., Ranasinghe, R., Huisman, B. A., Schipper, M. A., Swinkels, C. M., Walstra, D. J. R., & Stive, M. J. F. (2017). The initial morphological
620 response of the sand engine: a process-based modeling study. *Coastal Engineering*, (pp. 1–14).

Luijendijk, A. P., Scheel, F., Braat, L., & Waagmeester, N. (2015). Pilot application of Delft3D Flexible Mesh: Assisting a field campaign at the Sand Engine. In *E-proceedings of the 36th IAHR World Congress*. International
625 Association for Hydro-Environment Engineering and Research.

Maas, L., & Van Haren, J. (1987). Observations on the vertical structure of tidal and inertial currents in the central north sea. *Journal of Marine Research*, *45*, 293–318.

Nielsen, P., Callaghan, D. P., & Baldock, T. E. (2011). Downward transfer
630 of momentum by wind-driven waves. *Coastal Engineering*, *58*, 1118–1124.

Odgaard, A. J. (1986). Meander flow model. I: Development. *Journal of Hydraulic engineering*, .

- Radermacher, M., de Schipper, M. A., Swinkels, C., MacMahan, J. H.,
& Reniers, A. J. (2016). Tidal flow separation at protruding beach
635 nourishments. *Journal of Geophysical Research: Oceans*, . URL: <http://dx.doi.org/10.1002/2016JC011942>. doi:10.1002/2016JC011942.
- Raye, R. E., & Driscoll, F. R. (2002). Inertial correction of ship-mounted
ADCP records. In F. H. Maltz (Ed.), *Proceedings Oceans 2002 (Biloxi,
MS)*. Ocean Engineering Society.
- 640 de Schipper, M. A., de Vries, S., Ruessink, G., de Zeeuw, R. C., Rutten,
J., van Gelder-Maas, C., & Stive, M. J. (2016). Initial spreading of a
mega feeder nourishment: Observations of the Sand Engine pilot project.
Coastal Engineering, *111*, 23–38.
- Seim, H. E., & Gregg, M. C. (1997). The importance of aspiration and
645 channel curvature in producing strong vertical mixing over a sill. *Journal
of Geophysical Research: Oceans*, *102*, 3451–3472. URL: <http://dx.doi.org/10.1029/96JC03415>. doi:10.1029/96JC03415.
- Simpson, J., & Souza, A. (1995). Semidiurnal switching of stratification in
the region of freshwater influence of the Rhine. *Journal of Geophysical
650 Research*, *100*, 7037–7044.
- Simpson, J., Williams, E., Brasseur, L., & Brubaker, J. (2005).
The impact of tidal straining on the cycle of turbulence in a
partially stratified estuary. *Continental Shelf Research*, *25*, 51
– 64. URL: <http://www.sciencedirect.com/science/article/pii/>

655 S0278434304002122. doi:<http://dx.doi.org/10.1016/j.csr.2004.08.003>.

Simpson, J. H., Bos, W. G., Schirmer, F., Souza, A. J., Rippeth, T. P., Jones, S. E., & Hydes, D. (1993). Periodic stratification in the Rhine ROFI in the north sea. *Oceanologica Acta*, *16*, 23–32.

660 Souza, A., & Simpson, J. (1996). The modification of tidal ellipses by stratification in the Rhine ROFI. *Continental Shelf Research*, *16*, 997–1007.

Souza, A. J., & James, I. D. (1996). A two-dimensional (x- z) model of tidal straining in the Rhine ROFI. *Continental Shelf Research*, *16*, 949–966.

665 Souza, A. J., & Simpson, J. H. (1997). Controls on stratification in the Rhine ROFI system. *Journal of Marine Systems*, *12*, 311–323.

Stelling, G. S., & Van Kester, J. A. T. M. (1994). On the approximation of horizontal gradients in sigma co-ordinates for bathymetry with steep bottom slopes. *International Journal for Numerical Methods in Fluids*, *18*, 915–935.

670 Stive, M. J. F., de Schipper, M. A., Luijendijk, A. P., Aarninkhof, S. G. J., van Gelder-Maas, C., van Thiel de Vries, J. S. M., de Vries, S., Henriquez, M., Marx, S., & Ranasinghe, R. (2013). A new alternative to saving our beaches from sea-level rise: The sand engine. *Journal of Coastal Research*, *29*, 1001–1008.

675 Thomson, R. E., & Emery, W. J. (2014). *Data analysis methods in physical oceanography*. Newnes.

- Valle-Levinson, A., Huguenard, K., Ross, L., Branyon, J., MacMahan, J.,
& Reniers, A. (2015). Tidal and nontidal exchange at a subtropical in-
let: Destin inlet, northwest florida. *Estuarine, Coastal and Shelf Sci-*
680 *ence*, 155, 137 – 147. URL: [http://www.sciencedirect.com/science/
article/pii/S0272771415000414](http://www.sciencedirect.com/science/article/pii/S0272771415000414). doi:[http://dx.doi.org/10.1016/j.
ecss.2015.01.020](http://dx.doi.org/10.1016/j.ecss.2015.01.020).
- Van Rijn, L. (1997). Sediment transport and budget of central coastal zone
of holland. *Coastal Engineering*, 32, 61–90.
- 685 Visser, A., Souza, A., Hessner, K., & Simpson, J. (1994). The effect of
stratification on tidal current profiles in a region of fresh-water influence.
Oceanologica acta, 17, 369–381.
- Wijnberg, K. M. (2002). Environmental controls on decadal morpho-
logic behaviour of the holland coast. *Marine Geology*, 189, 227–
690 247. URL: [http://www.sciencedirect.com/science/article/pii/
S0025322702004802](http://www.sciencedirect.com/science/article/pii/S0025322702004802). doi:[http://dx.doi.org/10.1016/S0025-3227\(02\)
00480-2](http://dx.doi.org/10.1016/S0025-3227(02)00480-2).

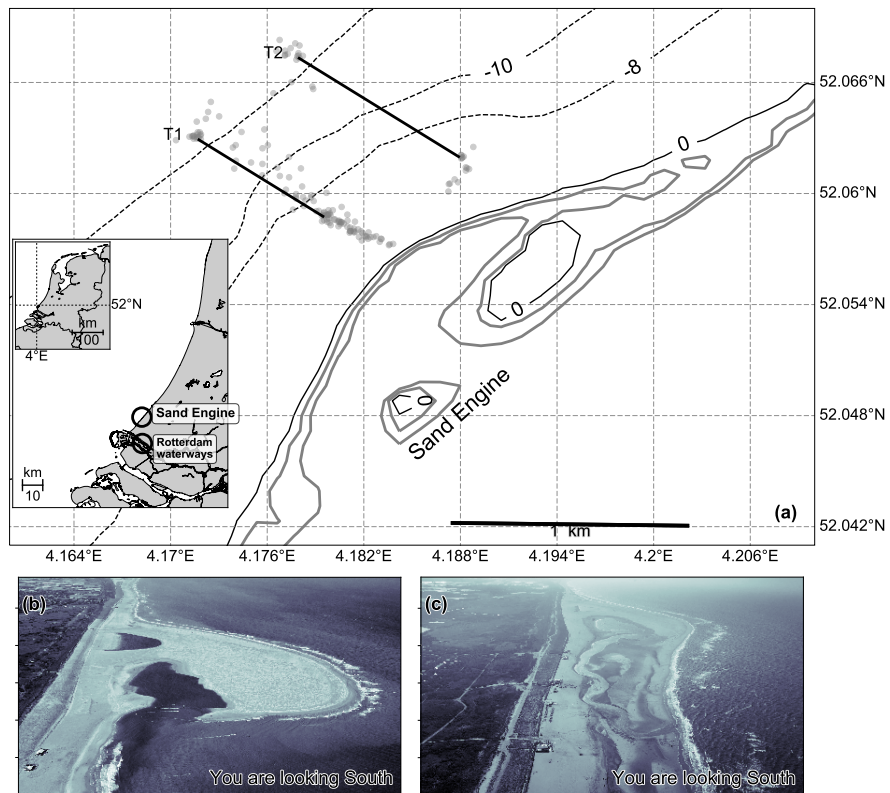


Figure 1: Study area location. (a) The inset shows the Netherlands within the Holland Coast with the Sand Engine and the Rotterdam waterways; (b) the Sand Engine a few months after its completion; and (c) the Sand Engine during the field experiment in Sep 2014 (Courtesy of Rijkswaterstaat/Joop van Houdt). The transects crossed the isobaths from -12 to -8 m, approximately. The gray circles show the location of the 153 CTD casts.

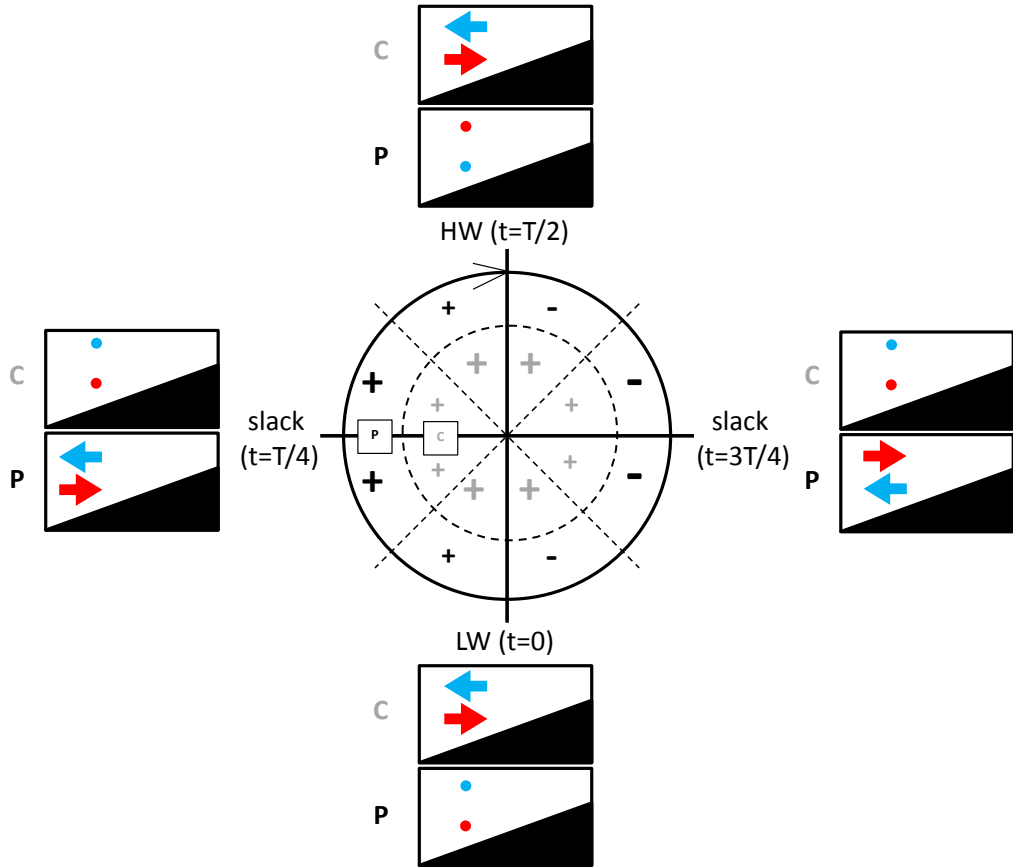


Figure 2: Idealized interplay between baroclinic pressure gradient (P) and centrifugal acceleration (C) along a cross-shore profile off the tip of the Sand Engine. The plus and minus signs indicate positive and negative vertical shear in the cross-shore (see text for explanation), their colors indicate the terms P (black) and C (gray) and their sizes indicate the magnitude. The panels show the cross-shore distribution of the cross-shore exchange currents generated by P and C. Blue arrows are offshore-directed and red arrows are onshore-directed. The colored dots indicate the cross-shore currents are nearly zero.

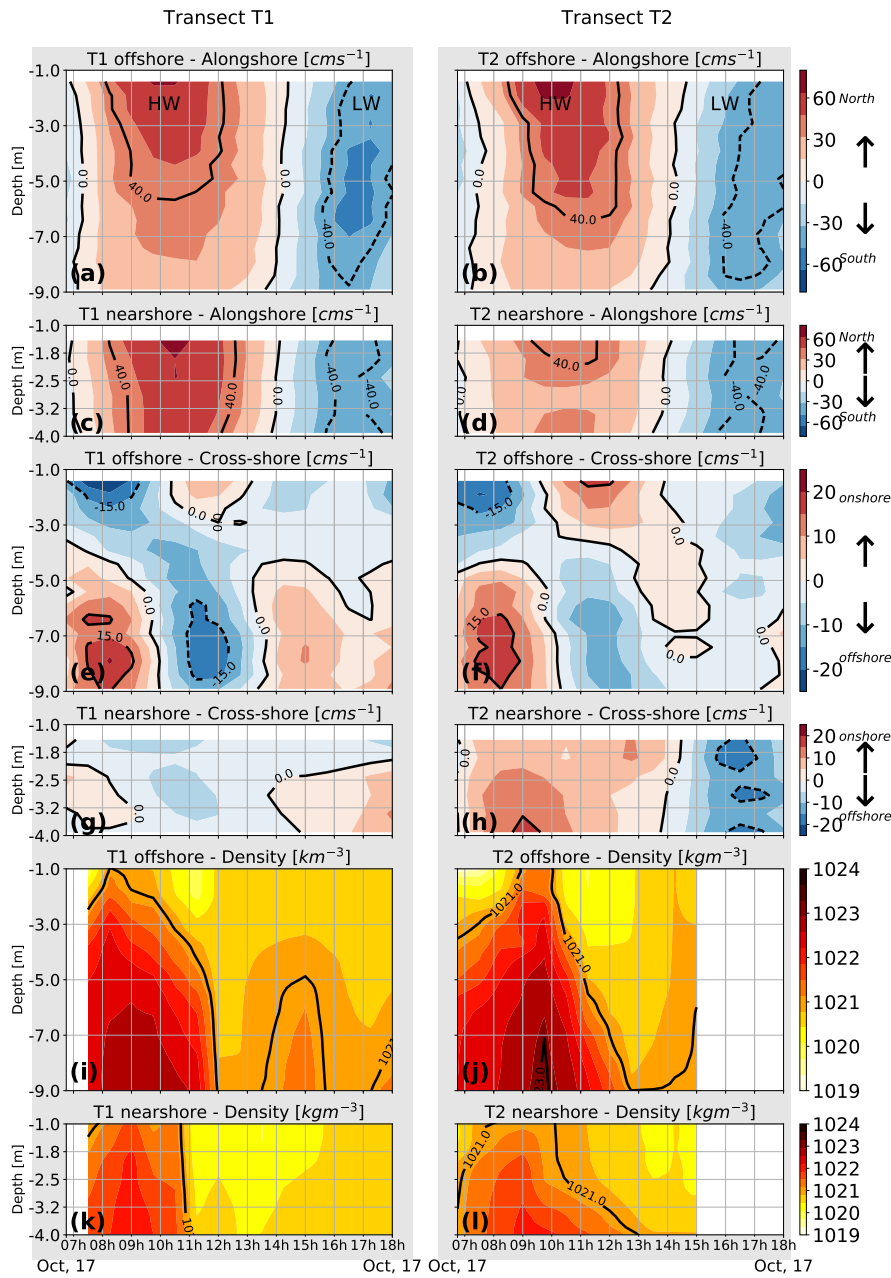


Figure 3: Time series of the observed cross- and alongshore profiles of the tidal velocities and density at the offshore (a, b, e, f, i and j) and onshore (c, d, g, h, k and l) limits of T1 (left) and T2 (right). The low water (LW) and high water (HW) tidal stages are indicated in (a) and (b). There is no CTD data after 1500H at T2 as seen by the blank space in (j) and (l).

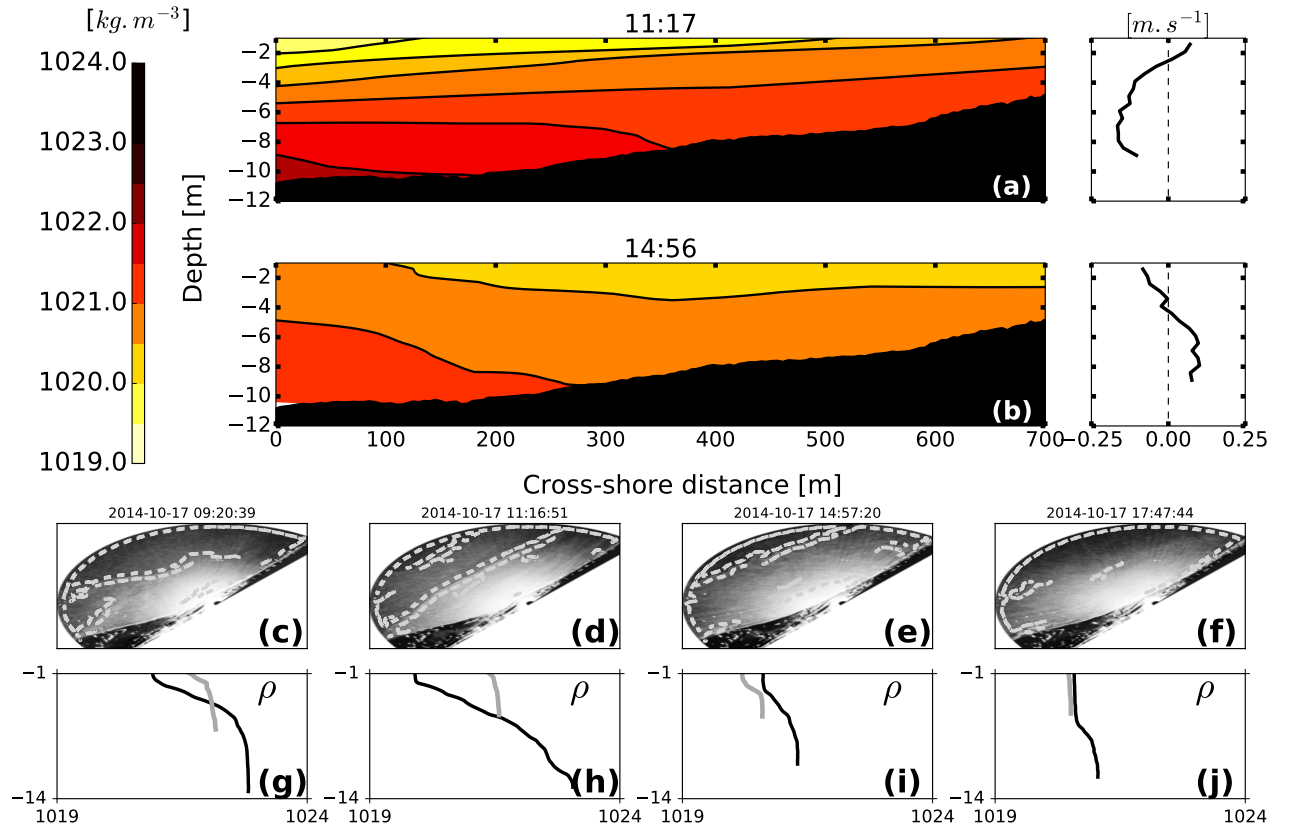


Figure 4: (a and b) Cross-shore density structure and the respective cross-shore velocity profiles at the seaward limit of T1. (c to f) Radar images of the Northern flank of the Sand Engine during four distinct periods of the survey. The contours in the images show the edge of the plume front. (g to j) Density profiles taken at the offshore (black line) and nearshore (gray line) limits of T1 for the same periods of the radar images.

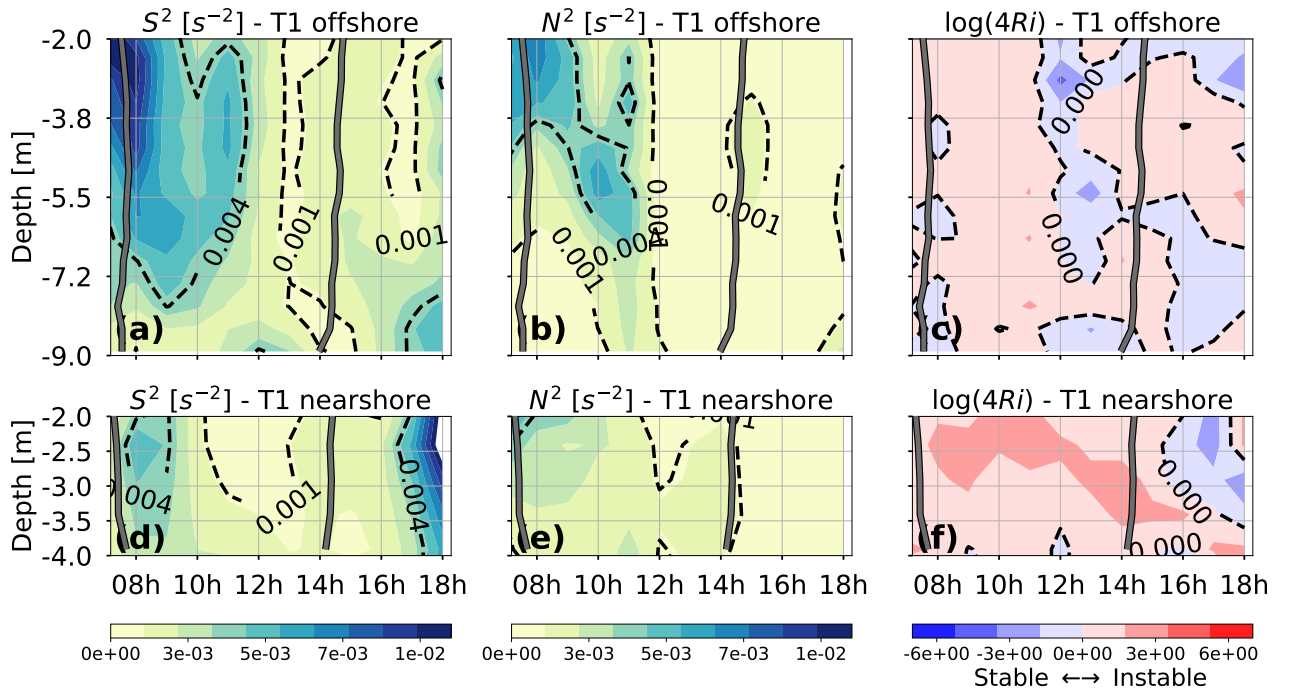


Figure 5: Time series of the squared vertical shear (S^2), buoyancy frequency (N^2) and the transformed Richardson Number ($\log(4Ri)$, where $Ri = N^2/S^2$) at the offshore (a, b and c) and onshore (d, e and f) limits of T1. The thick gray lines mark the HW and LW slacks (i.e, $v = 0$).

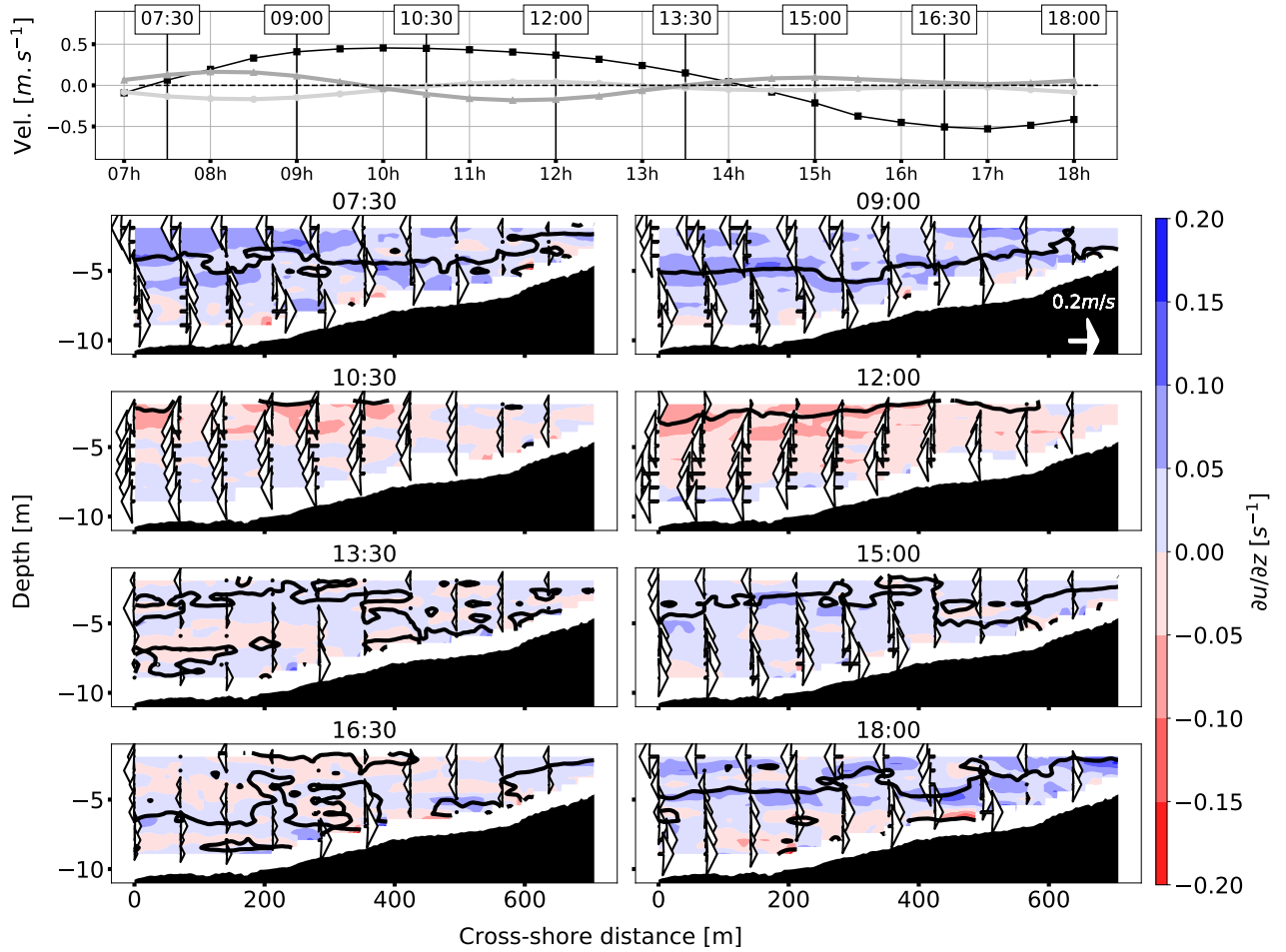


Figure 6: Upper panel: Depth-averaged alongshore (black line) velocity; and cross-shore near the bed (dark gray line) and near the surface (light gray line) velocities. The velocities were taken from the offshore limit of T1. Lower panel: vertical shear during 8 distinct periods over the tidal cycle. Negative values indicate a tendency to counterclockwise cross-shore circulation. The vectors represent the cross-shore velocities and the contour line indicates zero velocity.

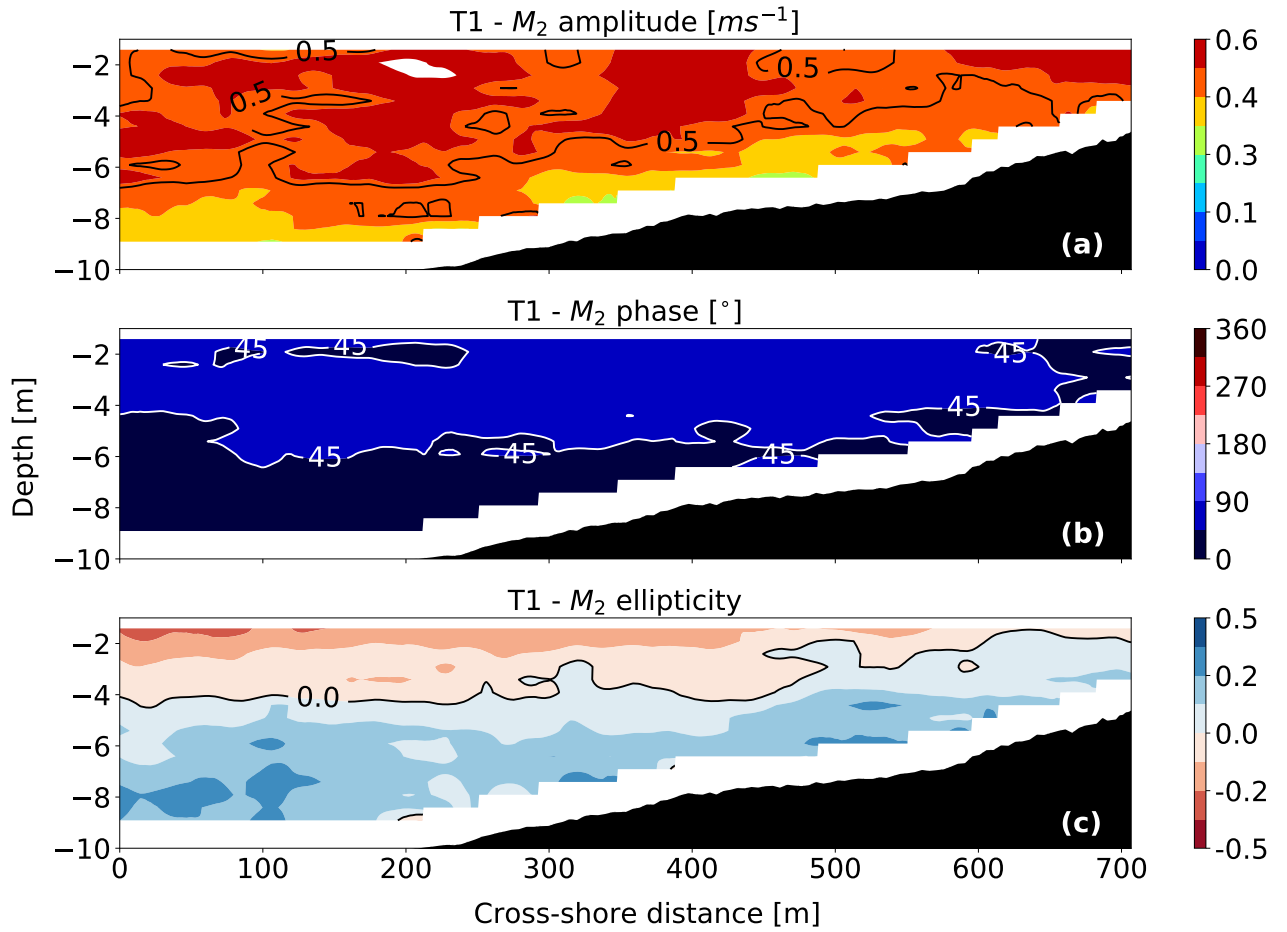


Figure 7: Main parameters of the M_2 tidal current ellipse at transect T1. (a) M_2 amplitude; (b) M_2 phase; (c) M_2 ellipticity.

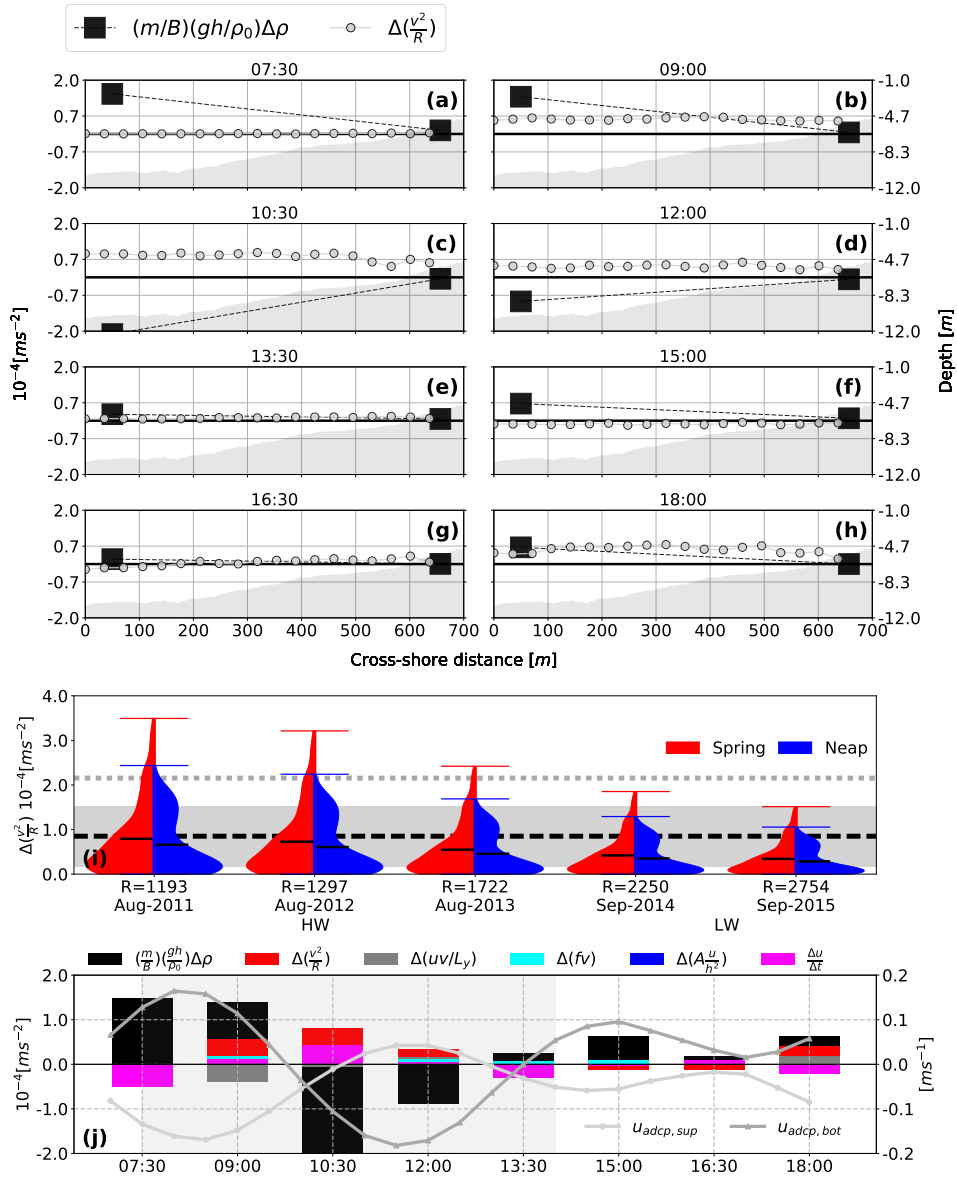


Figure 8: (a to h) Distribution of the baroclinic forcing (squares) and centrifugal acceleration (circles) along transect T1 during 8 distinct periods of the tidal cycle. (i) Violin plot of the estimated centrifugal acceleration off the tip of the Sand Engine considering the changes in the radius of curvature (R , in meters) from 2011 until 2015. The shapes correspond to the distribution of the data during spring (red) and neap (blue) with their respective maxima (colored bars) and means (black bars) values. The dashed black line and shaded area show the mean and standard deviation range of the baroclinic forcing. The dashed gray in (i) line indicates the maximum baroclinic forcing. (j) Scaled terms of the cross-shore exchange flow governing equation (left y-axis), and near surface and near bottom cross-shore velocities (right y-axis) at the seaward limit of T1.